Advanced Materials

ADVANCED MATERIALS
www.advmat.de

RESEARCH ARTICLE

Realization of Iodinene with Tunable Topological Edge States and Flat Bands

Dong Li[1,2] | Yu Wang[1,2] | Xinlei Zhao[3] | Jisong Gao[1,2] | Zhicheng Gao[1,2] | Yudian Zhou[1,2] | Yogendra Kumar[4] | Chenmin Liu[1,2] | Xuegao Hu[1,2] | Qiaoxiao Zhao[1,2] | Peng Cheng[1,2] | Masashi Arita[4] | Shin-ichiro Ideta[4] | Kenya Shimada[4] | Kehui Wu[5,8] | Yong Xu[3] | Lan Chen[1,2,6] | Baojie Feng[1,2,7,8]

[1]Institute of Physics, Chinese Academy of Sciences, Beijing, China | [2]School of Physical Sciences, University of Chinese Academy of Sciences, Beijing, China | [3]State Key Laboratory of Low Dimensional Quantum Physics and Department of Physics, Tsinghua University, Beijing, China | [4]Research Institute for Synchrotron Radiation Science (HiSOR), Hiroshima University, Higashi-Hiroshima, Japan | [5]Tsientang Institute for Advanced Study, Hangzhou, Zhejiang, China | [6]School of Physics, Hangzhou Normal University, Hangzhou, China | [7]Songshan Lake Materials Laboratory, Dongguan, Guangdong, China | [8]Interdisciplinary Institute of Light-Element Quantum Materials and Research Center For Light-Element Advanced Materials, Peking University, Beijing, China

Correspondence: Lan Chen (lchen@iphy.ac.cn) | Baojie Feng (bjfeng@iphy.ac.cn)

Received: 23 October 2025 | **Revised:** 13 February 2026 | **Accepted:** 17 February 2026

Keywords: angle-resolved photoemission spectroscopy | DFT calculations | iodinene | scanning tunneling microscopy | topological crystalline insulator

ABSTRACT

Halogens, known for their diatomic molecular structures, typically do not form extended covalent materials. The development of 2D elemental materials from halogens is therefore significant for both fundamental research and practical applications. Here, we report the realization of a monolayer iodine sheet, namely iodinene, with multiple exotic properties. Using angle-resolved photoemission spectroscopy, scanning tunneling microscopy, and first-principles calculations, we show that iodinene hosts 2D topological crystalline insulator states, a long-sought topological state previously observed only in 3D materials. Moreover, iodinene is exceptionally stable under ambient conditions. By applying a tensile strain of 48%, we realize two nearly flat bands with robust topological edge states in between, paving the way for the design and fabrication of tunable topological and spintronic devices.

1 | Introduction

Monoelemental 2D materials beyond graphene, known as Xenes, have garnered significant attention over the past decade [1–4]. Due to their intriguing physical, chemical, and biological properties, Xenes are considered promising materials for optoelectronic and spintronic devices, biomedical applications, and high-capacity batteries. To date, various Xenes—including those derived from Group III to Group VI elements and even transition metals—have been successfully synthesized, such as borophene [5, 6], silicene [7, 8], stanene [9, 10], bismuthene [11, 12], tellurene [13, 14], molybdenene [15], and goldene [16]. However, these materials often suffer from rapid degradation in air, limiting their ex situ characterization and hindering practical applications. For instance, silicene field-effect transistors degrade within just 2 min in air despite their notable carrier mobility [17]. Although borophene exhibits some resistance to oxidation, a significant portion can still be rapidly oxidized [6]. Furthermore, the limited range of exotic properties in most Xenes restricts their application in multifunctional quantum devices.

To overcome these challenges, a promising strategy is to synthesize Xenes from materials with high electronegativity and strong spin-orbit coupling (SOC), such as halogens. Under standard

Dong Li, Yu Wang and Xinlei Zhao contributed equally to this work.

conditions, most halogens are gases, making the synthesis of solid-state Xenes challenging. Iodine, however, is a notable exception, as it maintains its crystalline phase under ambient conditions. Its reactivity and polarizability make it essential in organic synthesis, catalysis, and halogen bonding, enabling advancements in pharmaceuticals, supramolecular chemistry, and crystal engineering. Recently, few-layer iodinene nanosheets have been synthesized via liquid-phase exfoliation [18–21]. These nanosheets have shown promise for applications such as high-rate ion batteries [18, 19] and antibacterial therapies, including treatments for bacterial wound infections and pneumonia [20, 21]. However, monolayer iodinene with covalent bonding has not yet been realized, and the electronic properties of iodinene remain largely unexplored. Theoretical calculations predict several monolayer iodinene structures stabilized by halogen bonding and diatomic molecular arrangements, exhibiting exotic properties such as nontrivial topology, flat bands, and remarkable optical characteristics [22, 23]. Recently, a honeycomb iodinene structure has been reported by a mild liquid-phase method under ambient conditions, but its intriguing electronic structure has not been experimentally investigated [24].

Topological crystalline insulators (TCIs) [25–28] represent a novel class of quantum materials where topological protection arises from crystalline symmetries rather than time-reversal symmetry, as is the case in conventional topological insulators. Consequently, TCIs offer robust electronic properties under a wide range of conditions, such as in the presence of magnetic fields or symmetry-conserving lattice distortions [29]. Moreover, TCIs support multiple Dirac cones, providing opportunities for the hybridization of Majorana zero modes when interfaced with superconductors [30]. To date, however, experimental work has predominantly focused on 3D TCIs. In the 2D limit, TCIs exhibit even more exotic properties [31–35], including gate-controllable Fermi levels, electric-field-tunable band gaps [31], and large-Chern-number quantum anomalous Hall effects [32], and strain-tunable topological phase transitions [34]. Nevertheless, the experimental realization of 2D TCIs remains challenging due to the limited availability of suitable material candidates.

Here, we report the realization of monolayer iodinene on Au(111) using molecular beam epitaxy (MBE). We investigated its atomic and electronic structures through scanning tunneling microscopy/spectroscopy (STM/S) and angle-resolved photoemission spectroscopy (ARPES), supported by first-principles calculations. Remarkably, iodinene exhibits exceptional air stability and several unprecedented properties, including 2D TCI states, high strain tolerance without altering its topological characteristics, and strain-tunable flat bands.

2 | Results

2.1 | DFT Calculations of Freestanding Iodinene

Freestanding iodinene has a triangular lattice with space group P6/mmm, where each iodine atom is covalently bonded to six nearest neighbors, as illustrated in Figure 1a. After full structural relaxation, the lattice constant is determined to be $a = 3.37$ Å, indicating that this geometry corresponds to a local minimum on the potential-energy surface for freestanding iodinene. Figure 1b depicts the band structures without and with SOC, respectively. In the absence of SOC, the two highest valence bands are degenerate at the Γ point and along the M-K-Γ path; these degeneracies are lifted when SOC is included. However, the SOC-induced gap is not global due to the dispersive nature of these bands, which can be viewed as an insulator defined on a curved Fermi level, as indicated by the grey shaded regions in Figure 1b. Applying tensile strain reduces the bandwidth of each band, potentially leading to the formation of a global gap. Figure S1 presents the calculated band structures for various lattice constants, demonstrating the expected gradual decrease in bandwidth with increasing tensile strain. When the lattice constant reaches 5.0 Å, corresponding to a tensile strain of approximately 48%, the bandwidth decreases by an order of magnitude, and only a slightly negative gap remains according to Perdew-Burke-Ernzerhof (PBE) functional calculations, as shown in Figure 1c. We will show later that a global gap exists when iodinene is grown on Au(111), which is essential for the detection of the topological edge states (TESs) discussed subsequently. Notably, the bands still exhibit finite dispersion, indicating the persistence of the I—I bonds.

Since the freestanding monolayer iodinene possesses mirror symmetry M_z, its topology can be classified using the mirror Chern number $C_{M_z} = (C_{+i} - C_{-i})/2$ [26, 31, 36, 37] where $C_{\pm i}$ are the Chern numbers for the eigenstates with $M_z = \pm i$. We employed the Wilson loop method [38, 39] to compute C_{M_z} for the lowest four occupied bands. Our calculations show that $C_{M_z} = 2$, as illustrated in Figure 1d, indicating the presence of two pairs of counter-propagating, spin-polarized TESs within the gap. We calculated the TESs of iodinene with $a = 5.0$ Å, which form two Dirac cones along the (01) edge (the x direction) and the $(2\bar{1})$ edge (the y direction), as shown in Figure S2. On the projected (01) edge, two pairs of counter-propagating TESs with opposite mirror eigenvalues are clearly visible, which connect two energy bands and intersect, forming two Dirac points along the $\bar{\Gamma} - \bar{X} - \bar{\Gamma}$ line. On the projected $(2\bar{1})$ edge, two pairs of TESs intersect at the $\bar{Y}$ point and subsequently merge into the bulk states along the $\bar{\Gamma} - \bar{Y} - \bar{\Gamma}$ direction. Moreover, there is no band crossing or inversion with changes in the lattice constant, suggesting that the nontrivial topology in the iodinene is robust against tensile strain. Thus, we conclude that the freestanding iodinene belongs to the topological crystalline insulator phase with $C_{M_z} = 2$ and possesses two pairs of helical edge states.

2.2 | Epitaxial Growth of Iodinene on Au(111)

The adsorption of halogen atoms on noble metal surfaces has been extensively studied over the past decades [40]. For example, the I/Au(111) system can be prepared by depositing a dilute solution of iodine in methanol [41]. We develop a method for synthesizing a high-quality iodine monolayer on Au(111) by directly evaporating nickel diiodide (NiI_2) under ultra-high vacuum conditions. Since the decomposition temperature of NiI_2 is lower than the evaporation temperature of the NiI_2 molecules, we can ensure the growth of pure iodine without Ni contaminants, as confirmed by our X-ray photoemission spectroscopy measurements (Figure S4). Remarkably, we find that the resulting iodine monolayer forms a covalently bonded 2D material—iodinene—rather than a simple adsorbed layer.

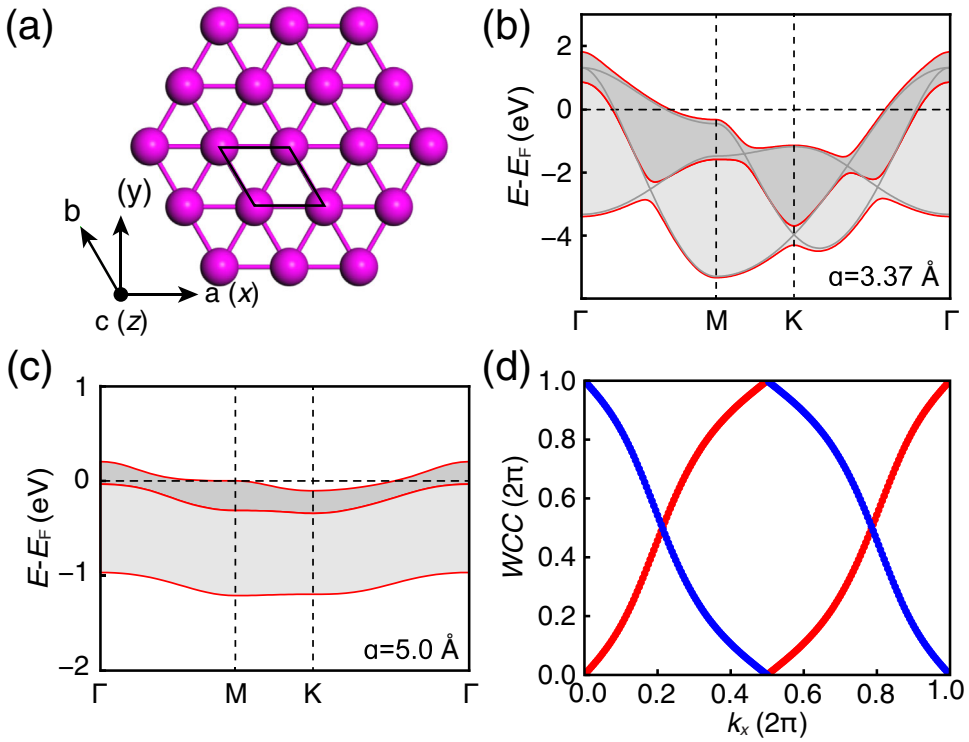

FIGURE 1 | Atomic and electronic structures of iodinene. (a) Schematic illustration of the atomic structure of freestanding iodinene. The black rectangle denotes a unit cell. (b) Calculated band structures of optimized freestanding iodinene without (grey) and with (red) SOC. The optimized lattice constant is 3.37 Å. (c) Calculated band structure of iodinene with a lattice constant of 5 Å, including SOC. (d) Wannier charge centers for $M_z = +i$ (red) and $M_z = -i$ (blue) eigenstates. The grey shaded regions in (b) and (c) indicate the SOC-induced band gaps.

When the iodine coverage reaches approximately one-third of a monolayer, a well-ordered iodinene monolayer covers the entire surface, accompanied by the disappearance of the $22 \times \sqrt{3}$ herringbone reconstruction characteristic of pristine Au(111). A high-resolution STM image, Figure 2a, reveals a triangular lattice with a lattice constant of 5.0 Å, corresponding to a $(\sqrt{3} \times \sqrt{3})$R30° superstructure ($\sqrt{3}$-iodinene), which is further confirmed by low-energy electron diffraction (LEED) measurements, as shown in Figure S5f. Figure 2c shows the atomic structure of the $\sqrt{3}$-iodinene, and each protrusion in the high-resolution STM image corresponds to one iodine atom. Remarkably, iodinene on Au(111) exhibits excellent air stability. LEED patterns and ARPES spectra show negligible degradation of iodinene after exposure to air (Figures S6 and S7). The stability of iodinene is also confirmed by AFM and STM measurements; after air exposure, the iodinene remains unchanged, and negligible adsorbates are observed. The air stability might originate from the high electronegativity and strong bonding of iodine atoms.

Given that freestanding iodinene has a lattice constant of 3.37 Å, the $\sqrt{3}$ iodinene on Au(111) experiences a tensile strain of approximately 48%. When the iodine coverage exceeds one-third of a monolayer, the $\sqrt{3}$-iodinene transitions into a striped phase with higher iodine density, due to the relaxation of tensile strain through uniaxial compression. This transition is consistent with the system relieving the high strain toward the freestanding structure. As the coverage increases, the spacing between stripes decreases, leading to a denser stripe pattern until a saturated striped phase is achieved. This entire process is monitored by STM and LEED, as shown in Figure S5. The saturated striped phase has a period of 15 Å × 4.98 Å, corresponding to a $5 \times \sqrt{3}$ superstructure, as shown in Figure 2b,d.

The evolution of the striped phase with increasing iodine coverage suggests that the distance between nearest-neighbor iodine atoms can be tuned quasi-continuously, offering opportunities to study the electronic structure as a function of strain. Interestingly, upon moderate annealing of the saturated stripe phase, the period of iodinene gradually increases and eventually reverts to the $\sqrt{3}$-iodinene. This behavior indicates that iodinene with a lattice constant of 5.0 Å is the most stable phase on Au(111).

2.3 | ARPES Measurements of the Band Structure

ARPES measurements were performed to investigate the electronic structure of iodinene. After the growth of iodinene, the Shockley surface state of Au(111) disappears, and only the folded bulk *sp* bands are observed within 1.5 eV below the Fermi level, as shown in Figure 3a–c. At higher binding energies, two nearly flat bands appear along the Γ–M direction of iodinene, as indicated by black arrows in Figure 3c. These two bands show negligible dispersion when measured with different photon energies (Figure S8), indicating weak hybridization between the electronic states of Au and iodinene. The weak hybridization is reasonable, as the interaction between iodine and gold is among the weakest in halogen-metal systems [40]. This is further supported by our X-ray photoemission spectroscopy

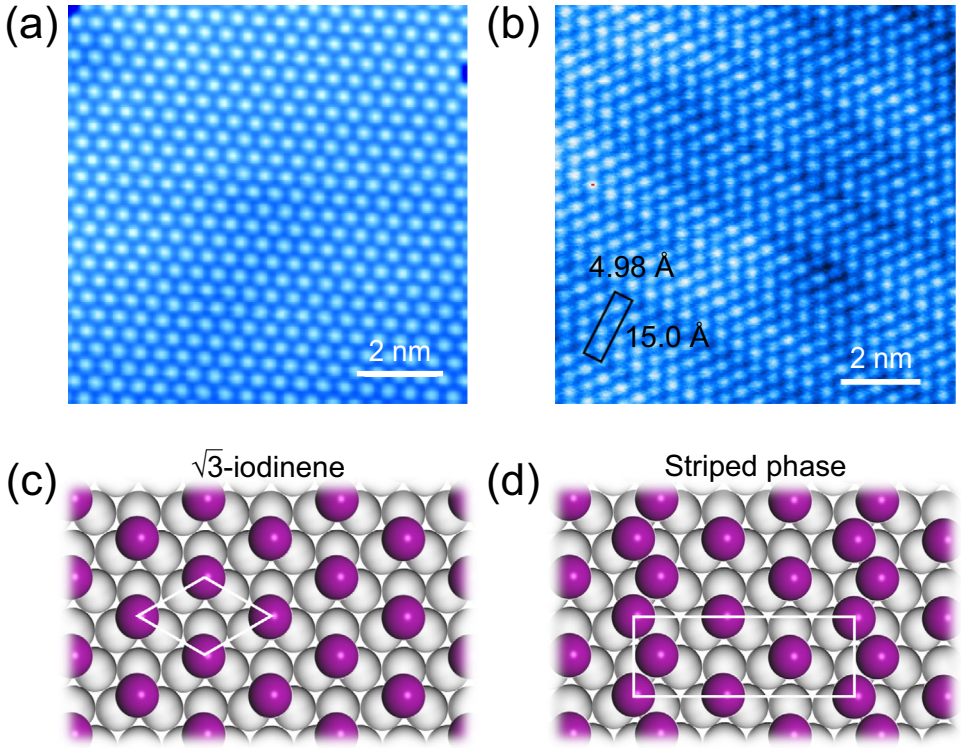

FIGURE 2 | Growth of iodinene on Au(111). (a,b) STM images of $\sqrt{3}$-iodinene and the saturated striped phase on Au(111). (c,d) Atomic structural models of $\sqrt{3}$-iodinene (c) and the striped phase (d). Purple and grey balls represent I and Au atoms, respectively. The striped phase consists of both strained and unstrained $\sqrt{3}$-iodinene regions.

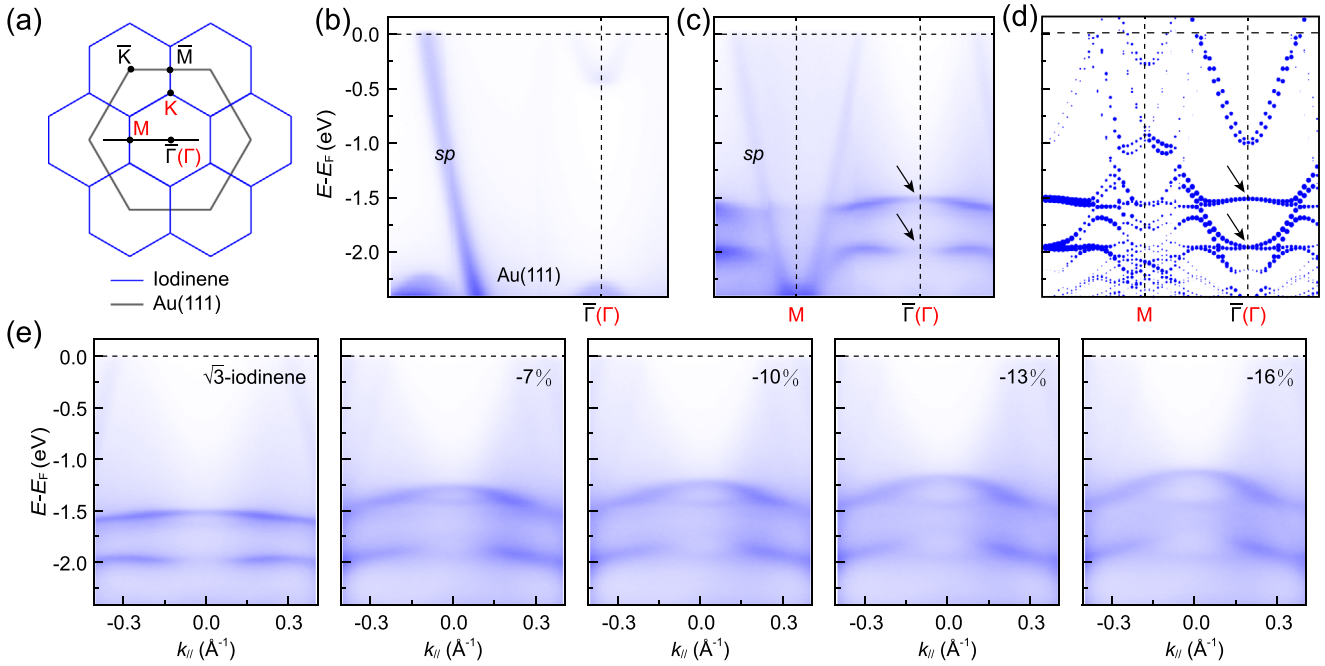

FIGURE 3 | ARPES measurements of iodinene. (a) Schematic drawing of the BZs of $\sqrt{3}$-iodinene and Au(111), respectively. (b,c) ARPES intensity plots along the $\bar{K} - \bar{\Gamma} - \bar{K}$ direction of Au(111) for pristine Au(111) and $\sqrt{3}$-iodinene, respectively. (d) Unfolded band structures of $\sqrt{3}$-iodinene, including the substrate. SOC was included in the calculations. The marker size represents the spectral weight projected onto the iodine atoms. (e) ARPES intensity plots of the striped phases. The strain values, relative to the $\sqrt{3}$-iodinene are indicated in each panel.

measurements (Figure S9). Both bands are nearly flat near the Γ point at binding energies of 1.6 and 2 eV, respectively, and exhibit slight downward dispersion halfway along the Γ–M direction, forming hole-like pockets in the constant energy contours (Figure S10). These bands are symmetric with respect to the M point of iodinene, consistent with its periodicity. Notably, the two nearly flat bands have a global gap, making it feasible to detect the TESs.

To understand the electronic structure of iodinene, we performed first-principles calculations including the Au(111) substrate. Using an orbital-selective band unfolding technique, we unfolded the effective band structures of the iodinene/Au(111) system onto the first Brillouin zone (BZ) of Au(111), as shown in Figure 3d and Figure S11. The calculated band structures along the $\bar{\Gamma}-\bar{\mathrm{K}}$ direction of Au(111) was projected onto the atomic orbitals of iodine to compare with the ARPES data. Our results show excellent agreement with the ARPES measurements. Further calculations reveal that the two nearly flat bands derive from the *p* orbitals of iodine atoms (Figure S12). Notably, these findings are also consistent with the calculated band structures of freestanding iodinene shown in Figure 1c. This suggests a weak hybridization between the nearly flat bands of iodinene and the Au(111) substrate. At the same time, significant charge transfer occurs at the interface, indicating strong chemical bonding between iodine and Au, which is essential for imposing the large tensile strain on iodinene.

We then conducted ARPES measurements on the striped phase, which corresponds to iodinene with varying tensile strains, as discussed earlier. The ARPES data are presented in Figure 3e. As the iodine coverage increases or the lattice constant decreases, the two nearly flat bands near the Γ point gradually become more dispersive until the saturated striped phase is formed. Notably, the nearly flat bands remain observable in the striped phase, although their intensity is significantly weaker compared to the $\sqrt{3}$-iodinene, suggesting the non-uniform nature of the stripe phase, as illustrated by the structural model in Figure 2d.

2.4 | Topological Edge States of Iodinene

Since the non-trivial band topological properties and the bulk-edge correspondence in iodinene, TESs are expected to exist at arbitrary edges. In unstrained iodinene, the absence of a global bandgap and interference from bulk bands make it difficult to detect TESs using scanning tunneling spectroscopy (STS). However, our ARPES measurements demonstrate that a global bandgap exists in $\sqrt{3}$-iodinene, making it suitable for measuring edge states. The differential conductance ($\mathrm{d}I/\mathrm{d}V$) curves acquired on a flat terrace of $\sqrt{3}$-iodinene are shown by the blue line in Figure 4a. Two prominent peaks were observed at 1.59 eV and 1.95 eV, respectively, corresponding to the two nearly flat bands observed in our ARPES measurements Figure 3c. The $\mathrm{d}I/\mathrm{d}V$ curves taken near the edges reveal an increase in spectral weight between these two peaks, as shown by the red lines in Figure 4a and Figure S13, indicating the presence of in-gap edge states. This behavior is in good agreement with the calculated local density of states, as shown in Figure 4b.

Next, we investigated the spatial distribution of the TESs through a series of $\mathrm{d}I/\mathrm{d}V$ maps on $\sqrt{3}$-iodinene with a step edge of Au(111), as shown in Figure 4c1–c5. A trivial edge state is located directly at the atomic edges over a wide energy range, as indicated by the black arrow in Figure 4c. However, an additional unique edge state appears on both the upper and lower terraces, slightly away from the atomic edges, as indicated by the red arrows. This state is only observed from −1.70 to 1.85 eV, which is between the two nearly flat bands, in contrast to the trivial edge states that exist over a wider energy range. For comparison, we performed STS measurements on the striped phase, and the results are shown in Figure 4d1–d5. As expected, neither the gap nor the edge states were observed due to the lack of a global bandgap.

To further confirm the robustness of the edge states, we studied a submonolayer $\sqrt{3}$-iodinene with irregular holes, as shown in Figure 4e1–e4. The $\mathrm{d}I/\mathrm{d}V$ maps display additional spectral weight around the holes at energies from −1.70 to −1.80 eV, corresponding to the TESs, as indicated by the red arrows. This observation suggests that the edge states are independent of the crystalline orientation, consistent with their topological origin. Notably, the edge states were observed around the edges of the holes, while the interiors, being bare Au(111), did not exhibit such states. Collectively, our findings provide solid evidence for the existence of TESs in $\sqrt{3}$-iodinene, suggesting the nontrivial topological nature of iodinene.

It should be noted that the mirror symmetry M_z is broken when iodinene is grown on Au(111), as one side of the iodinene layer interfaces with the substrate while the other faces vacuum. Generally, breaking mirror symmetry would result in the opening of a band gap at the Dirac points formed by the TESs of a 2D TCI. However, we did not observe such a gap within our experimental resolution, likely due to the weak band hybridization between iodinene and Au(111). On the other hand, for the gapless Dirac points at time-reversal invariant momenta [such as the $\bar{\mathrm{Y}}$ point shown in Figure S2], the band crossings are simultaneously protected by time-reversal symmetry and mirror symmetry M_z. These band crossings would be destroyed only if both symmetries are broken. Therefore, the TESs of iodinene are preserved on Au(111).

The mirror symmetry M_z, which protects the TESs of iodinene, can be broken by applying a perpendicular electric field. Therefore, it is feasible to induce band gaps in the TESs through an external electric field. This indicates that the conductance of iodinene can be precisely controlled via electric fields, in addition to the gate voltages used in conventional 2D materials. Similar properties have been predicted in other 2D TCIs such as $Pb_{1-x}Sn_xSe(Te)$ [31] and Sb/Bi honeycomb structures [42, 43]. This mechanism can achieve high on/off speeds and power efficiency [44]. In contrast, achieving an energy gap in a quantum spin Hall insulator typically requires external magnetic fields or induced ferromagnetism, both of which present challenges [45]. Additionally, because the spin polarization in the *z* direction is proportional to the M_z eigenvalue, the electric current carried by the TESs of iodinene is spin polarized. Reversing the direction of the current will also reverse the spin polarization, indicating a full entanglement of charge and spin transport [31]. Therefore, it is possible to realize a topological transistor device where charge

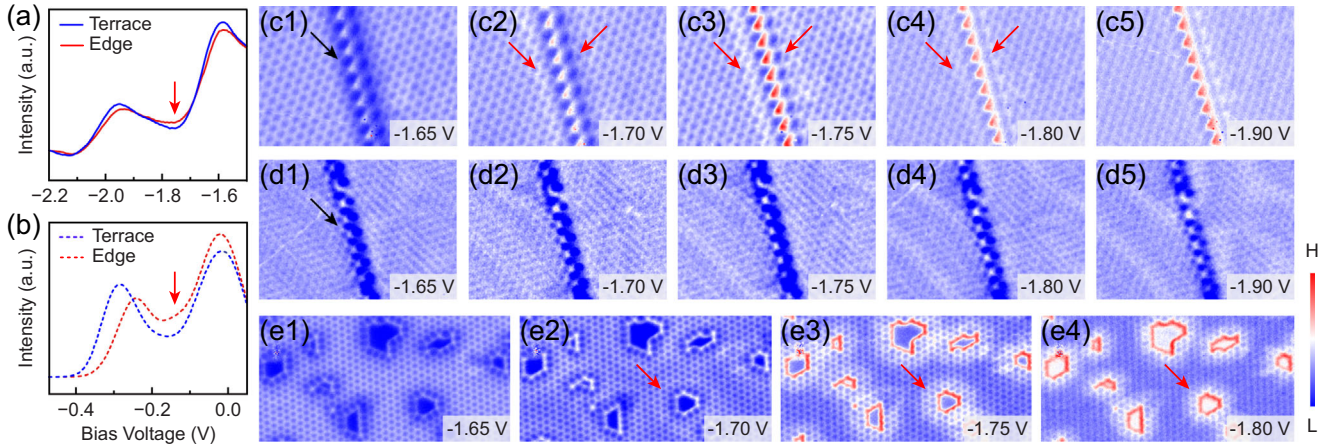

FIGURE 4 | Topological edge states of iodinene. (a) dI/dV spectra acquired on a flat terrace (blue) and at a step edge (red), respectively. The data were normalized by I/V. (b) Calculated density of states of bulk (blue) and edge (red) atoms in freestanding nanoribbons. (c1)–(c5) and (d1)–(d5) dI/dV mappings of $\sqrt{3}$-iodinene and the striped phase across step edges, respectively. (e1)–(e4) dI/dV mappings of $\sqrt{3}$-iodinene on an area with irregular holes. Black and red arrows indicate trivial and topological edge states, respectively.

and spin transport can be simultaneously controlled by an electric field.

In summary, we present compelling experimental and theoretical evidence for monolayer iodinene, a material that hosts multiple exotic properties—including air stability, symmetry-protected topological edge states, and strain-tunable flat electronic bands. Beyond the discovery of a new elemental 2D material, our work introduces a substrate-enabled strategy to simultaneously stabilize the lattice and engineer nontrivial band topology and electronic correlations in the 2D limit. These findings not only deepen the understanding of 2D topological materials but also establish iodinene as a versatile platform for exploring robust edge transport and flat-band physics, opening pathways toward designing multifunctional quantum devices.

3 | Experimental Section

3.1 | Sample Preparation

Iodinene samples were prepared in an MBE chamber with a base pressure better than 1×10^{-10} mbar. Iodine atoms were evaporated from a NiI_2 source onto Au(111) substrates at room temperature. The NiI_2 source temperature was maintained at 500 and 650 K for the growth of iodinene and NiI_2, respectively. Prior to growth, the Au(111) substrates were cleaned by repeated argon ion sputtering and annealing cycles. The quality of the samples was confirmed by LEED, STM, and ARPES measurements.

3.2 | ARPES and STM Measurements

ARPES measurements were performed using both laboratory and synchrotron facilities. Three light sources were employed: a helium discharge lamp (He Iα radiation), a 10.8 eV *p*-polarized laser [46], and synchrotron radiation. The samples were maintained at 70 K during measurements. The base pressure during ARPES measurements was approximately 1×10^{-10} mbar.

STM experiments were conducted using a home-built low-temperature STM. All topographic images and scanning tunneling spectroscopy spectra were acquired at 5 K using a chemically etched tungsten tip. The bias voltages were defined as the sample bias with respect to the tip. The dI/dV spectra were measured with a modulation voltage of 20 mV at 667 Hz. Atomic force microscopy (AFM) measurements were conducted using a commercial scanning probe microscope (Asylum Research Cypher S, Oxford Instruments) at room temperature in ambient conditions.

3.3 | Theoretical Calculations

First-principles calculations were carried out by using density functional theory (DFT) together with the projector augmented wave (PAW) method [47, 48] as implemented in the Vienna ab initio simulation package (VASP) [49, 50]. The Perdew-Burke-Ernzerhof type exchange correlation functional [51] was employed. The energy cutoff of the plane wave basis was set to 500 eV. The Brillouin zone was sampled by the Monkhorst-Pack method in the self-consistent process with a 12 × 12 × 1 *k*-mesh. The thickness of the vacuum along the *z*-direction was set to >20 Å. The phonon spectrum was calculated using a finite displacement approach as implemented in the PHONOPY code [52]. The maximally localized Wannier functions for the I *p* orbitals were constructed using the Wannier90 package [53]. The edge spectra were calculated using the surface Green's function of a semi-infinite system [54, 55], as implemented in the WannierTools package [39]. Wannier charge centers were calculated using the WannierTools package [39].

Acknowledgements

We thank Professor Zhijun Wang for insightful discussions. This work was supported by the National Key R&D Program of China (Grants Nos. 2024YFA1408400, 2024YFA1408700, and 2024YFA1409100), the Beijing Natural Science Foundation (Grant Number JQ23001), the National

Natural Science Foundation of China (Grants No. W2411004, T2325028, 12374197, 12134019, 12304239, 12334003, 12421004, and 12361141826), the CAS Project for Young Scientists in Basic Research (Grants No. YSBR-047 and YSBR-054), the Postdoctoral Fellowship Program of CPSF (Grants No. GZB20230829 and GZC20231369), and the China Postdoctoral Science Foundation (Grants No. 2023TQ0367, 2023TQ0174, and 2024M761599). Y.W. acknowledges the support from the Special Research Assistant Program of the Chinese Academy of Sciences. Synchrotron ARPES measurements were carried out with the approval of the Proposal Assessing Committee under Proposal Nos. 23BG041 and 23BG042 at the Research Institute for Synchrotron Radiation Science, Hiroshima University, Japan. The calculations were performed at the National Supercomputer Center in Tianjin using the Tianhe new generation supercomputer.

Conflicts of Interest

The authors declare no conflicts of interest.

Data Availability Statement

The data that support the findings of this study are available from the corresponding author upon reasonable request.

References

1. A. Molle and C. Grazianetti, *Xenes: 2D Synthetic Materials beyond Graphene*, (Elsevier, 2022).

2. W. Tao, N. Kong, X. Ji, et al., "Emerging Two-dimensional Monoelemental Materials (Xenes) for Biomedical Applications," *Chemical Society Reviews* 48 (2019): 2891–2912, https://doi.org/10.1039/C8CS00823J.

3. A. J. Mannix, B. Kiraly, M. C. Hersam, and N. P. Guisinge, "Synthesis and Chemistry of Elemental 2D Materials," *Nature Reviews Chemistry* 1 (2017): 0014, https://doi.org/10.1038/s41570-016-0014.

4. A. Molle, J. Goldberger, M. Houssa, Y. Xu, S.-C. Zhang, and D. Akinwande, "Buckled Two-Dimensional Xene Sheets," *Nature Materials* 16 (2017): 163–169, https://doi.org/10.1038/nmat4802.

5. A. J. Mannix, X.-F. Zhou, B. Kiraly, et al., "Synthesis of Borophenes: Anisotropic, Two-Dimensional Boron Polymorphs," *Science* 350 (2015): 1513–1516, https://doi.org/10.1126/science.aad1080.

6. B. Feng, J. Zhang, Q. Zhong, et al., "Experimental Realization of Two-Dimensional Boron Sheets," *Nature Chemistry* 8 (2016): 563–568, https://doi.org/10.1038/nchem.2491.

7. P. Vogt, P. De Padova, C. Quaresima, et al., "Silicene: Compelling Experimental Evidence for Graphene like Two-Dimensional Silicon," *Physical Review Letters* 108 (2012): 155501, https://doi.org/10.1103/PhysRevLett.108.155501.

8. B. Feng, Z. Ding, S. Meng, et al., "Evidence of Silicene in Honeycomb Structures of Silicon on Ag(111)," *Nano Letters* 12 (2012): 3507–3511, https://doi.org/10.1021/nl301047g.

9. F.-F. Zhu, W.-J. Chen, Y. Xu, et al., "Epitaxial Growth of Two-Dimensional Stanene," *Nature Materials* 14 (2015): 1020–1025, https://doi.org/10.1038/nmat4384.

10. J. Deng, B. Xia, X. Ma, et al., "Epitaxial Growth of Ultraflat Stanene With Topological Band Inversion," *Nature Materials* 17 (2018): 1081–1086, https://doi.org/10.1038/s41563-018-0203-5.

11. F. Reis, G. Li, L. Dudy, et al., "Bismuthene on a SiC Substrate: A Candidate for a High-Temperature Quantum Spin Hall Material," *Science* 357 (2017): 287–290, https://doi.org/10.1126/science.aai8142.

12. R. Stühler, F. Reis, T. Müller, et al., "Tomonaga–Luttinger Liquid In The Edge Channels Of A Quantum Spin Hall Insulator," *Nature Physics* 16 (2020): 47–51, https://doi.org/10.1038/s41567-019-0697-z.

13. Y. Wang, G. Qiu, R. Wang, et al., "Field-Effect Transistors Made From Solution-Grown Two-Dimensional Tellurene," *Nature Electronics* 1 (2018): 228–236, https://doi.org/10.1038/s41928-018-0058-4.

14. Z. Zhu, X. Cai, S. Yi, et al., "Multivalency-Driven Formation of Te-based Monolayer Materials: A Combined First-Principles and Experimental Study," *Physical Review Letters* 119 (2017): 106101, https://doi.org/10.1103/PhysRevLett.119.106101.

15. T. K. Sahu, N. Kumar, S. Chahal, et al., "Microwave Synthesis of Molybdenene From MoS_2," *Nature Nanotechnology* 18 (2023): 1430–1438, https://doi.org/10.1038/s41565-023-01484-2.

16. S. Kashiwaya, Y. Shi, J. Lu, et al., "Synthesis of Goldene Comprising Single-atom Layer Gold," *Nature Synthesis* 3 (2024): 744–751, https://doi.org/10.1038/s44160-024-00518-4.

17. L. Tao, E. Cinquanta, D. Chiappe, et al., "Silicene Field-Effect Transistors Operating at Room Temperature," *Nature Nanotechnology* 568 (2019): 216–220.

18. M. Qian, Z. Xu, Z. Wang, et al., "Realizing Few-Layer Iodinene for High-Rate Sodium-Ion Batteries," *Advanced Materials* 32 (2020): 2004835, https://doi.org/10.1002/adma.202004835.

19. C. Kuang, W. Zeng, M. Qian, and X. Liu, "Liquid-Phase Exfoliated Few-Layer Iodine Nanosheets for High-Rate Lithium-Iodine Batteries," *ChemPlusChem* 86 (2021): 865–869, https://doi.org/10.1002/cplu.202100166.

20. Y. You, Y.-X. Zhu, J. Jiang, et al., "Iodinene Nanosheet-to-iodine Molecule Allotropic Transformation for Antibiosis," *Journal of the American Chemical Society* 145 (2023): 13249–13260, https://doi.org/10.1021/jacs.3c02669.

21. Y. Ye, Y. Wang, K. Zhang, et al., "Facile Fabrication Of Two-Dimensional Iodine Nanosheets For Antibacterial Therapy," *Biomaterials Science* 11 (2023): 1311–1317, https://doi.org/10.1039/D2BM01763F.

22. K. Yu, Y. Liu, B. Fu, et al., "Design Monolayer Iodinenes Based on Halogen Bond and Tiling Theory," *Physical Review B* 109 (2024): 125423, https://doi.org/10.1103/PhysRevB.109.125423.

23. Z. Zhu, J. Gu, J. Gao, et al., "Structural Diversity and Topological Property of I-based Two-dimensional Inorganic Molecular Crystals," *Physical Review B* 108 (2023): 115409, https://doi.org/10.1103/PhysRevB.108.115409.

24. Y. Luo, C. Huang, X. Han, et al., "Metallic Monolayer Iodinene Sheets," *Matter* 8 (2025): 102157.

25. L. Fu, "Topological Crystalline Insulators," *Physical Review Letters* 106 (2011): 106802, https://doi.org/10.1103/PhysRevLett.106.106802.

26. T. H. Hsieh, H. Lin, J. Liu, W. Duan, A. Bansil, and L. Fu, "Topological Crystalline Insulators in the SnTe Material Class," *Nature Communications* 3 (2012): 982, https://doi.org/10.1038/ncomms1969.

27. Y. Tanaka, Z. Ren, T. Sato, et al., "Experimental Realization of a Topological Crystalline Insulator in SnTe," *Nature Physics* 8 (2012): 800–803, https://doi.org/10.1038/nphys2442.

28. P. Dziawa, B. J. Kowalski, K. Dybko, et al., "Topological Crystalline Insulator States in $Pb_{1-x}Sn_xSe$," *Nature Materials* 11 (2012): 1023–1027, https://doi.org/10.1038/nmat3449.

29. Y. Ando and L. Fu, "Topological Crystalline Insulators and Topological Superconductors: From Concepts to Materials," *Annual Review of Condensed Matter Physics* 6 (2015): 361–381, https://doi.org/10.1146/annurev-conmatphys-031214-014501.

30. T. Liu, C. Y. Wan, H. Yang, et al., "Signatures of Hybridization of Multiple Majorana Zero Modes in a Vortex," *Nature* 633 (2024): 71–76, https://doi.org/10.1038/s41586-024-07857-4.

31. J. Liu, T. H. Hsieh, P. Wei, W. Duan, J. Moodera, and L. Fu, "Spin-Filtered Edge States With an Electrically Tunable Gap in a Two-Dimensional Topological Crystalline Insulator," *Nature Materials* 13 (2014): 178–183, https://doi.org/10.1038/nmat3828.

32. C. Fang, M. J. Gilbert, and B. A. Bernevig, "Large-Chern-Number Quantum Anomalous Hall Effect in Thin-Film Topological Crystalline Insulators," *Physical Review Letters* 112 (2014): 046801, https://doi.org/10.1103/PhysRevLett.112.046801.

33. J. Liu, X. Qian, and L. Fu, "Crystal Field Effect Induced Topological Crystalline Insulators In Monolayer IV–VI Semiconductors," *Nano Letters* 15 (2016): 2657–2661, https://doi.org/10.1021/acs.nanolett.5b00308.

34. C. Niu, P. M. Buhl, G. Bihlmayer, D. Wortmann, S. Blügel, and Y. Mokrousov, "Two-dimensional Topological Crystalline Insulator and Topological Phase Transition in TlSe and TlS Monolayers," *Nano Letters* 15 (2015): 6071–6075, https://doi.org/10.1021/acs.nanolett.5b02299.

35. S. Liu, A. Vishwanath, and E. Khalaf, "Shift Insulators: Rotation-protected Two-Dimensional Topological Crystalline Insulators," *Physical Review X* 9 (2019): 031003, https://doi.org/10.1103/PhysRevX.9.031003.

36. J. C. Y. Teo, L. Fu, and C. L. Kane, "Surface States And Topological Invariants In Three-Dimensional Topological Insulators: Application to $Bi_{1-x}Sb_x$," *Physical Review B* 78 (2008): 045426, https://doi.org/10.1103/PhysRevB.78.045426.

37. H. Weng, J. Zhao, Z. Wang, Z. Fang, and X. Dai, "Topological Crystalline Kondo Insulator in Mixed Valence Ytterbium Borides," *Physical Review Letters* 112 (2014): 016403, https://doi.org/10.1103/PhysRevLett.112.016403.

38. R. Yu, X. L. Qi, A. Bernevig, Z. Fang, and X. Dai, "Equivalent Expression of Z_2 Topological Invariant for Band Insulators Using the Non-Abelian Berry Connection," *Physical Review B* 84 (2011): 075119, https://doi.org/10.1103/PhysRevB.84.075119.

39. Q. Wu, S. Zhang, H.-F. Song, M. Troyer, and A. A. Soluyanov, "WannierTools: An Open-source Software Package for Novel Topological Materials," *Computer Physics Communications* 224 (2018): 405–416, https://doi.org/10.1016/j.cpc.2017.09.033.

40. B. V. Andryushechkin, T. V. Pavlova, and K. N. Eltsov, "Adsorption of Halogens on Metal Surfaces," *Surface Science Reports* 73 (2018): 83–115, https://doi.org/10.1016/j.surfrep.2018.03.001.

41. L. Huang, P. Zeppenfeld, S. Horch, and G. Comsa, "Determination of Iodine Adlayer Structures on Au(111) by Scanning Tunneling Microscopy," *The Journal of Chemical Physics* 107 (1997): 585–591, https://doi.org/10.1063/1.474419.

42. C.-H. Hsu, Z.-Q. Huang, C. P. Crisostomo, et al., "Two-Dimensional Topological Crystalline Insulator Phase in Sb/Bi Planar Honeycomb With Tunable Dirac Gap," *Scientific Reports* 6 (2016): 18993, https://doi.org/10.1038/srep18993.

43. Y. Yin, C. Wang, M. S. Fuhrer, and N. V. Medhekar, "Extracting Unconventional Spin Texture in Two Dimensional Topological Crystalline Insulator Bismuthene via Tuning Bulk-Edge Interactions," *Materials Today Physics* 36 (2023): 101168, https://doi.org/10.1016/j.mtphys.2023.101168.

44. M. Lang, L. He, X. Kou, et al., "Competing Weak Localization and Weak Antilocalization in Ultrathin Topological Insulators," *Nano Letters* 13 (2013): 48–53, https://doi.org/10.1021/nl303424n.

45. L. Du, I. Knez, G. Sullivan, and R.-R. Du, "Robust Helical Edge Transport in Gated InAs/GaSb Bilayers," *Physical Review Letters* 114 (2015): 096802, https://doi.org/10.1103/PhysRevLett.114.096802.

46. J. Gao, Q. Zhao, W. Liu, et al., "Development of a 10.8-eV Table-top Femtosecond Laser With Tunable Polarization for High-Resolution Angle-Resolved Photoemission Spectroscopy," *Review Of Scientific Instruments* 96 (2025): 093004, https://doi.org/10.1063/5.0268243.

47. P. E. Blöchl, "Projector Augmented-Wave Method," *Physical Review B* 50 (1994): 17953–17979.

48. G. Kresse and D. Joubert, "From Ultrasoft Pseudopotentials to the Projector Augmented-Wave Method," *Physical Review B* 59 (1999): 1758–1775, https://doi.org/10.1103/PhysRevB.59.1758.

49. G. Kresse and J. Furthmüller, "Efficiency of Ab-initio Total Energy Calculations for Metals and Semiconductors Using a Plane-wave Basis Set," *Computational Materials Science* 6 (1996): 15–50, https://doi.org/10.1016/0927-0256(96)00008-0.

50. G. Kresse and J. Furthmüller, "Efficient Iterative Schemes for Ab Initio Total-energy Calculations Using a Plane-wave Basis Set," *Physical Review B* 54 (1996): 11169–11186, https://doi.org/10.1103/PhysRevB.54.11169.

51. J. P. Perdew, K. Burke, and M. Ernzerhof, "Generalized Gradient Approximation Made Simple," *Physical Review Letters* 77 (1996): 3865–3868, https://doi.org/10.1103/PhysRevLett.77.3865.

52. A. Togo and I. Tanaka, "First Principles Phonon Calculations in Materials Science," *Scripta Materialia* 108 (2015): 1–5, https://doi.org/10.1016/j.scriptamat.2015.07.021.

53. N. Marzari, A. A. Mostofi, J. R. Yates, I. Souza, and D. Vanderbilt, "Maximally Localized Wannier Functions: Theory and Applications," *Reviews of Modern Physics* 84 (2012): 1419–1475, https://doi.org/10.1103/RevModPhys.84.1419.

54. M. P. L. Sancho, J. M. L. Sancho, J. M. L. Sancho, and J. Rubio, "Highly Convergent Schemes for the Calculation of Bulk and Surface Green Functions," *Journal of Physics F: Metal Physics* 15 (1985): 851–858, https://doi.org/10.1088/0305-4608/15/4/009.

55. M. P. L. Sancho, J. M. L. Sancho, and J. Rubio, "Quick Iterative Scheme for the Calculation of Transfer Matrices: Application to Mo (100)," *Journal of Physics F: Metal Physics* 14 (1984): 1205–1215, https://doi.org/10.1088/0305-4608/14/5/016.

Supporting Information

Additional supporting information can be found online in the Supporting Information section.

Supporting File: adma72637-sup-0001-SuppMat.docx.